



OPEN ACCESS

EDITED BY

Geeta Durga,
Sharda University, India

REVIEWED BY

Shichun Mu,
Wuhan University of Technology, China
Kezhen Qi,
Dali University, China

*CORRESPONDENCE

Wu Xia,
✉ chemxw_2008@163.com
Ao Yu,
✉ ao.yu@ucf.edu

RECEIVED 10 August 2025

ACCEPTED 13 October 2025

PUBLISHED 27 October 2025

CITATION

Huang T, Xia W, Joshua F, Ponnusamy VS,
Zhang Q, Kumar S and Yu A (2025) Interfacial
p–n coupling in Cu₃N/1T-MoS₂
heterojunctions drives efficient and durable
acidic hydrogen evolution.
Front. Energy Res. 13:1683318.
doi: 10.3389/fenrg.2025.1683318

COPYRIGHT

© 2025 Huang, Xia, Joshua, Ponnusamy,
Zhang, Kumar and Yu. This is an open-access
article distributed under the terms of the
[Creative Commons Attribution License \(CC
BY\)](https://creativecommons.org/licenses/by/4.0/). The use, distribution or reproduction in
other forums is permitted, provided the
original author(s) and the copyright owner(s)
are credited and that the original publication
in this journal is cited, in accordance with
accepted academic practice. No use,
distribution or reproduction is permitted
which does not comply with these terms.

Interfacial p–n coupling in Cu₃N/1T-MoS₂ heterojunctions drives efficient and durable acidic hydrogen evolution

Tianjiao Huang¹, Wu Xia^{1*}, Fnu Joshua²,
Vaishnavii Subbiah Ponnusamy², Qipeng Zhang²,
Sachin Kumar² and Ao Yu^{2*}

¹College of Chemistry and Chemical Engineering, Jishou University, Jishou, China, ²NanoScience Technology Center, University of Central Florida, Orlando, FL, United States

Rational interfacial engineering is crucial to designing non-precious electrocatalysts for the hydrogen evolution reaction (HER). Here we report a Cu₃N/1T-MoS₂ heterojunction in which ultrathin 1T-MoS₂ nanosheets are conformally grown on conductive p-type Cu₃N nanocubes. Spectroscopy and microscopy reveal intimate lattice contact and interfacial strain, while XPS indicates charge redistribution across the junction. In 0.5 M H₂SO₄, the optimized 1:1 composite delivers an overpotential of 387 mV at 50 mA cm⁻² and a Tafel slope of 57 mV dec⁻¹, outperforming both constituents (MoS₂ ≈ 456 mV; Cu₃N inactive at this current density). Continuous operation for 150 h demonstrates excellent acid stability. Electrochemical impedance and double-layer capacitance analyses show the lowest charge-transfer resistance and the highest electrochemically active surface area among all samples (C_{dl} = 103.6 mF cm⁻²), corroborating rapid electron transport and abundant accessible sites. The activity enhancement arises from a p–n heterojunction with a built-in field that promotes directional electron flow to MoS₂ active edges, together with strain-induced defect exposure. This work identifies Cu₃N as an effective platform to stabilize conductive MoS₂ and provides design rules for interface-engineered HER catalysts.

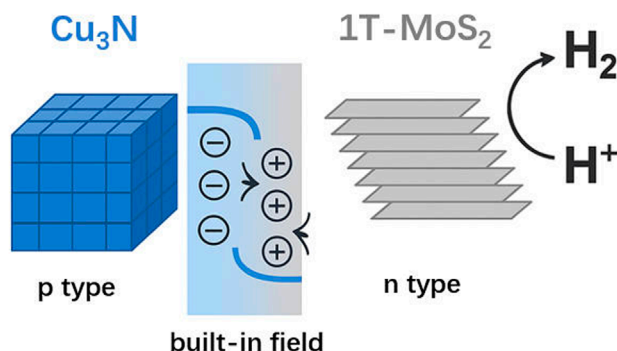
KEYWORDS

Cu₃N, 1T-MoS₂, p–n heterojunction, electrocatalytic hydrogen evolution, interfacial engineering

1 Introduction

Hydrogen is a versatile clean-energy carrier crucial for deep decarbonization across chemicals, transportation, and grid storage (Ayodele et al., 2019; Li et al., 2020; McHugh et al., 2020; Sun et al., 2023). Electrochemical water splitting (Sun Y. et al., 2021) offers a modular, high-purity route to hydrogen (H₂) when powered by renewables, but cost-effective deployment still requires non-precious electrocatalysts that combine low overpotentials, high current densities, and long-term

Interfacial p–n Coupling in Cu₃N/1T-MoS₂ Heterojunctions Drives Efficient and Durable Acidic Hydrogen Evolution



GRAPHICAL ABSTRACT

stability – requirements that remain a major challenge (Boretta et al., 2021; Li et al., 2016; Sun H. et al., 2021; Vasiliadou et al., 2018).

Among non-precious metal candidates, transition-metal dichalcogenides (TMDs) are promising for the hydrogen evolution reaction (HER) (Chia et al., 2015; Liu et al., 2019; Meshesha et al., 2023; Rao et al., 2021; Xue et al., 2022). Molybdenum disulfide (MoS₂) is particularly attractive owing to its tunable chemistry and edge-site activity, yet performance is constrained by the largely inert basal plane of semiconducting 2H-MoS₂ and by limited in-plane conductivity. Metallic 1T-MoS₂ improves conductivity and increases the population of active sites, but it is metastable under operating conditions and prone to activity decay (Amiin et al., 2017; Chiu et al., 2024). Conventional remedies – defect/phase engineering, heteroatom doping, and conductive supports – can accelerate kinetics but often compromise stability or require complex syntheses (Gong et al., 2023; Jin et al., 2025; Liu et al., 2020; Miao et al., 2024).

To overcome these limitations, we couple p-type copper nitride (Cu₃N) with 1T-MoS₂ (Kwon et al., 2025). Cu₃N is an attractive yet underexplored semiconductor with good conductivity, nitrogen-vacancy-rich cubic lattices, and a moderate work function (Gan et al., 2022; Wang et al., 2023; Zhang et al., 2021; Zhu et al., 2020a), enabling rapid carrier transport and scalable synthesis, enabling a p-n heterojunction with a built-in field that directs electrons to MoS₂ edge sites while extracting holes into Cu₃N, thereby enhancing charge separation and accelerating HER kinetics. Strong interfacial coupling further stabilizes the 1T phase of MoS₂, and favorable adsorption/transport characteristics support high-current, durable operation (Du et al., 2022; Jin et al., 2025; Wang et al., 2024). Compared with recent MoS₂-based heterojunctions (typically n-n or metal–semiconductor pairings, Supplementary Table S1), the Cu₃N/1T-MoS₂ architecture combines directional charge transfer, noble-metal-free electronic wiring, improved 1T-phase stability, and robust acidic performance.

In this work, Cu₃N/1T-MoS₂ achieves $\eta_{50} = 387$ mV (under 50 mA cm⁻² of current density) and a Tafel slope of 57 mV dec⁻¹

in 0.5 M H₂SO₄, maintaining performance for 150 h, demonstrating advantages in comprehensive performance. These results highlight the benefits of p-n interfacial coupling and the built-in field in funneling electrons to MoS₂ edge sites, delivering mechanism-anchored gains in both kinetics and durability, and offering a simple, non-precious route toward practical HER catalysts¹.

2 Materials and methods

2.1 Chemicals

All reagents were of analytical grade and used without further purification. Sodium hydroxide (NaOH, 95%) was purchased from Macklin Biochemical Technology Co., Ltd. Hydrochloric acid (HCl, 36%) and sulfuric acid (H₂SO₄, 98%) were obtained by Hunan Huihong Reagent Co., Ltd. Ammonium heptamolybdate tetrahydrate ((NH₄)₆Mo₇O₂₄·4H₂O, 99%) and thiourea (CH₄N₂S) were supplied from Sinopharm Chemical Reagent Co., Ltd. Copper (II) acetate monohydrate (Cu(OAc)₂·H₂O, 99%) and potassium hydroxide (KOH, 95%) were obtained from Aladdin Biochemical Technology Co., Ltd. Urea (CH₄N₂O, 99%) was acquired from Xilong Scientific Co., Ltd.

2.2 Synthesis of Cu₃N

Cu₃N was synthesized via a chemical vapor deposition route. Specifically, 0.33 g of Cu(OAc)₂·H₂O and 0.50 g of urea were separately placed in two porcelain boats. The precursors were heated to 300 °C at a ramp rate of 5 °C·min⁻¹ under a continuous Ar flow (40

¹ For Original Research articles, please note that the Material and Methods section can be placed in any of the following ways: before Results, before Discussion or after Discussion

sccm) and maintained for 2 h. After cooling to room temperature, the black powder was collected, washed with deionized water (3×50 mL) and ethanol (3×50 mL) successively, and dried under vacuum at 60°C for 12 h (Mondal and Raj, 2018).

2.3 Synthesis of MoS_2

1T phase MoS_2 was synthesized following a modified hydrothermal procedure. Briefly, 1.25 g ammonium heptamolybdate tetrahydrate ($(\text{NH}_4)_6\text{Mo}_7\text{O}_{24}\cdot 4\text{H}_2\text{O}$, 1.0 mmol) and 2.28 g thiourea (30.0 mmol) were dissolved in 35 mL deionized water and stirred for 30 min. The homogeneous solution was transferred to a 100 mL Teflon-lined stainless-steel autoclave, sealed, and heated at 180°C for 24 h. After cooling, the resulting black precipitate was separated by centrifugation (6,000 rpm, 10 min per cycle), washed thoroughly with deionized water and ethanol, and vacuum-dried at 60°C for 12 h (Wang et al., 2020).

2.4 Synthesis of $\text{Cu}_3\text{N}/\text{MoS}_2$ composites

To synthesize the $\text{Cu}_3\text{N}/\text{MoS}_2$ (1:1) composite, 0.21 g of Cu_3N (1.0 mmol), 0.54 g $(\text{NH}_4)_6\text{Mo}_7\text{O}_{24}\cdot 4\text{H}_2\text{O}$ (0.43 mmol), and 0.98 g thiourea (12.87 mmol) were dispersed in 35 mL of deionized water with stirring for 30 min. The mixture was sealed in a 100 mL Teflon-lined autoclave and subjected to hydrothermal treatment at 180°C for 24 h. After natural cooling, the solid product was collected by centrifugation, washed with water and ethanol successively for three times, and dried under vacuum at 60°C for 12 h. Additional composites with $\text{Cu}_3\text{N}/\text{MoS}_2$ of 1:0.5 and 1:2 were prepared under identical conditions.

2.5 Electrode preparation

Catalyst inks were prepared by dispersing 2.5 mg of $\text{Cu}_3\text{N}/\text{MoS}_2$ powder in 400 μL ethanol and 90 μL deionized water, followed by ultrasonication to achieve a homogeneous suspension. Then, 10 μL of Nafion[®] 117 solution (~ 5 wt%) was added, and the mixture was sonicated again. A 6 μL aliquot of the resulting ink was drop-cast onto a glassy carbon electrode (GCE, 3 mm diameter), yielding a loading of ~ 0.4 mg cm^{-2} . The electrode was dried at ambient temperature prior to electrochemical testing.

2.6 Characterization

X-ray diffraction (XRD) was performed on a TD-3500 diffractometer using Cu K α radiation ($\lambda = 0.15406$ nm), scanned over a 2θ range of 5° – 90° with a scan rate of $2.4^\circ\cdot\text{min}^{-1}$. X-ray photoelectron spectroscopy (XPS) was carried out on a Thermo Scientific K-Alpha spectrometer equipped with an Al K α source ($h\nu = 1486.6$ eV). Scanning electron microscopy (SEM) and energy-dispersive X-ray spectroscopy (EDS) were conducted on a ZEISS Sigma 300 microscope using INLENS and ET detectors. Transmission electron microscopy (TEM) and EDS mapping

were conducted using a JEOL JEM-F200 system equipped with JED-2300T.

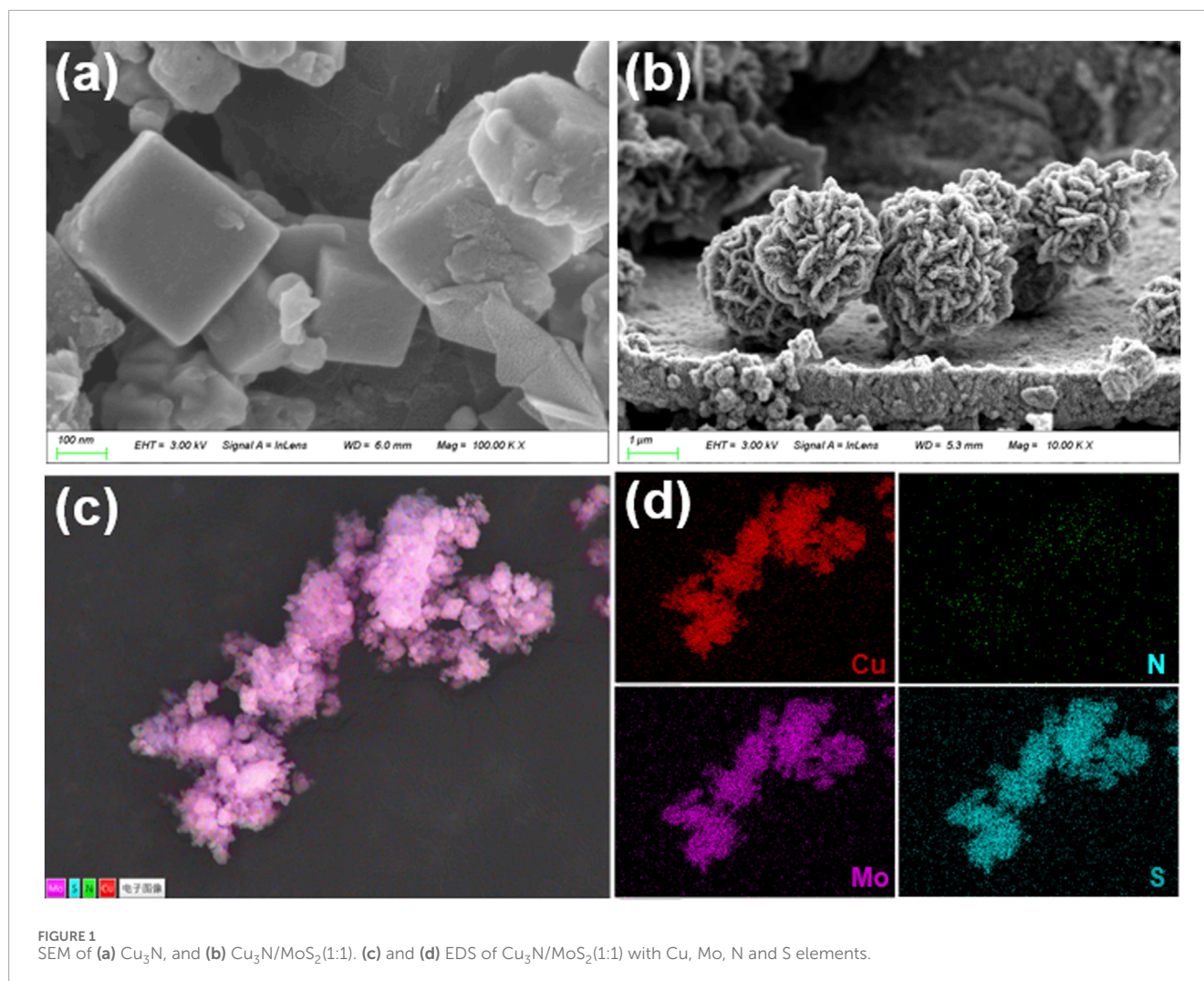
2.7 Electrochemical measurements

Electrochemical HER measurements were conducted in 0.5 M H_2SO_4 ($\text{pH} \approx 0.34$) using a three-electrode setup: the modified GCE as the working electrode, a graphite rod as the counter electrode, and an Ag/AgCl (3 M KCl) electrode as the reference. Linear sweep voltammetry (LSV) was recorded at 5 mV s^{-1} with 90% iR compensation. Potentials were converted to the reversible hydrogen electrode (RHE) scale using related formula ($E_{\text{RHE}} = E_{\text{Ag/AgCl}} + 0.0592 \text{ pH} + 0.197$ V). Tafel slopes were derived from LSV curves. Electrochemical impedance spectroscopy (EIS) was conducted at an overpotential of 387 mV over the frequency range of 0.1 Hz–100 kHz. The electrochemically active surface area (ECSA) was estimated from the double-layer capacitance (C_{dl}), obtained via cyclic voltammetry (CV) at scan rates of 5 – 25 mV s^{-1} within the non-Faradaic potential window (0.2175–0.3175 V vs. RHE).

3 Results and discussion

Scanning-electron-microscopy (SEM) images for pristine Cu_3N and for $\text{Cu}_3\text{N}/\text{MoS}_2$ composites obtained with Cu_3N -to-Mo precursors of 1:0.5, 1:1 and 1:2 are compiled, while the corresponding energy-dispersive X-ray spectroscopy (EDS) elemental maps for the 1:1 sample are presented in Figures 1c,d, Supplementary Figure S1B. The as-synthesized Cu_3N consists of smooth cubes. The narrow size distribution and sharp edges corroborate the phase purity inferred from XRD (Figure 2a) (Mallick et al., 2024; Mondal and Raj, 2018).

Introducing a limited amount of Mo precursor leads to the nucleation of ultrathin MoS_2 nanosheets directly on the Cu_3N cubes. The flakes anchor preferentially on the vertices and edges, giving rise to a rough texture while preserving the underlying cubic morphology (Figures 1a,b, Supplementary Figures S1C, D). At a stoichiometric precursor ratio, MoS_2 growth becomes self-sustaining, producing densely packed, radially oriented nanosheets that coalesce into rose-like microflowers (overall diameter 0.8–2 μm). Each flower encloses a Cu_3N core that is completely obscured by the MoS_2 shell, suggesting a core-shell or yolk-shell heterostructure (Chiu et al., 2024; Gong et al., 2023). The hierarchical porosity created by the inter-flake voids is expected to facilitate electrolyte infiltration and accelerate mass transport in electrocatalytic operation. Further increasing the Mo precursor leads to excessive MoS_2 deposition. Thick, entangled nanosheets (~ 20 nm) intergrow into open networks that protrude several hundred nanometers from the core. Although this architecture maximizes the content of MoS_2 , it may compromise electronic coupling to the Cu_3N core and partially block ion channels, underscoring the need for stoichiometric optimization (Supplementary Figures S1C, D). Element-specific signals for Cu, N, Mo and S are co-distributed throughout the 1:1 heterostructure. The Cu and N maps coincide with the core region, whereas Mo and S extend uniformly over the entire flower-like particle, confirming the conformal growth of MoS_2 on Cu_3N . No extraneous



elements are detected, attesting to the chemical integrity of the composite (Figures 1c,d). The systematic evolution from sparsely decorated cubes to fully encapsulated core-shell flowers demonstrates that MoS_2 nucleation and growth can be finely tuned by the $\text{Cu}_3\text{N}:\text{Mo}$ precursor ratio. These morphological attributes rationalize the superior electrochemical performance discussed in next section.

The crystal structures of Cu_3N , MoS_2 , and $\text{Cu}_3\text{N}/\text{MoS}_2$ heterojunction were analyzed by X-ray diffraction (XRD) (Figure 2a). Distinct reflections at 23.2° , 33.2° , 41.0° and 47.7° are assigned to the (100) (110), (111), and (200) planes of cubic Cu_3N (JCPDS No. 74-0242), confirming phase purity (Mallick et al., 2024; Mondal and Raj, 2018). The MoS_2 sample shows reflections at 33° , 49° , and 58° for the (100) (105), and (110) planes of the 1T phase, with additional peaks at 19° and 43° further indicating 1T formation. A broad basal reflection centred at 9.5° corresponds to an interlayer spacing of $d_{002} = 0.93$ nm, markedly larger than the 0.62 nm of bulk 2H- MoS_2 . Such expansion is characteristic of the 1T polymorph generated by chemical exfoliation or intercalation-driven electron injection (Jayabal et al., 2018; Wang et al., 2020; Yu et al., 2018). All fingerprint peaks of both parent lattices are retained in $\text{Cu}_3\text{N}/\text{MoS}_2$ composite, indicating that

hydrothermal assembly proceeds without alloying or oxide/sulfide by-products. The peak shifts of $\text{Cu}_3\text{N}(111)$ ($41.0^\circ \rightarrow 40.78^\circ$) and $\text{MoS}_2(100)$ ($33.0^\circ \rightarrow 33.26^\circ$), together with line broadening, indicate strong interfacial interactions between Cu_3N and MoS_2 , further corroborated by TEM and XPS analyses.

Transmission-electron microscopy (TEM) was employed to visualize the crystal architecture of pristine Cu_3N (Figure 2b) and of the $\text{Cu}_3\text{N}/\text{MoS}_2(1:1)$ heterostructures synthesised with $\text{Cu}_3\text{N}:\text{Mo}$ precursor ratios of 1:1 (Figure 2c). Low-magnification images reveal monodisperse nanocubes (Figure 2b). Lattice fringes of 0.19 nm assigned to the Cu_3N (200) planes extend coherently before intersecting with 0.32 nm fringes originating from the MoS_2 (100) planes (Figure 2d) (Jayabal et al., 2018; Mallick et al., 2024; Mondal and Raj, 2018; Wang et al., 2020; Yu et al., 2018). The acute intersection angle ($\approx 90^\circ$) reveals a semi-coherent interface, indicating epitaxial alignment despite the large symmetry mismatch between cubic Cu_3N and hexagonal MoS_2 . No amorphous halos or disordered fringe terminations are detected, indicating that the hydrothermal overgrowth does not induce grain-boundary amorphisation. The absence of misfit dislocations within the examined field further supports coherent, low-defect bonding.

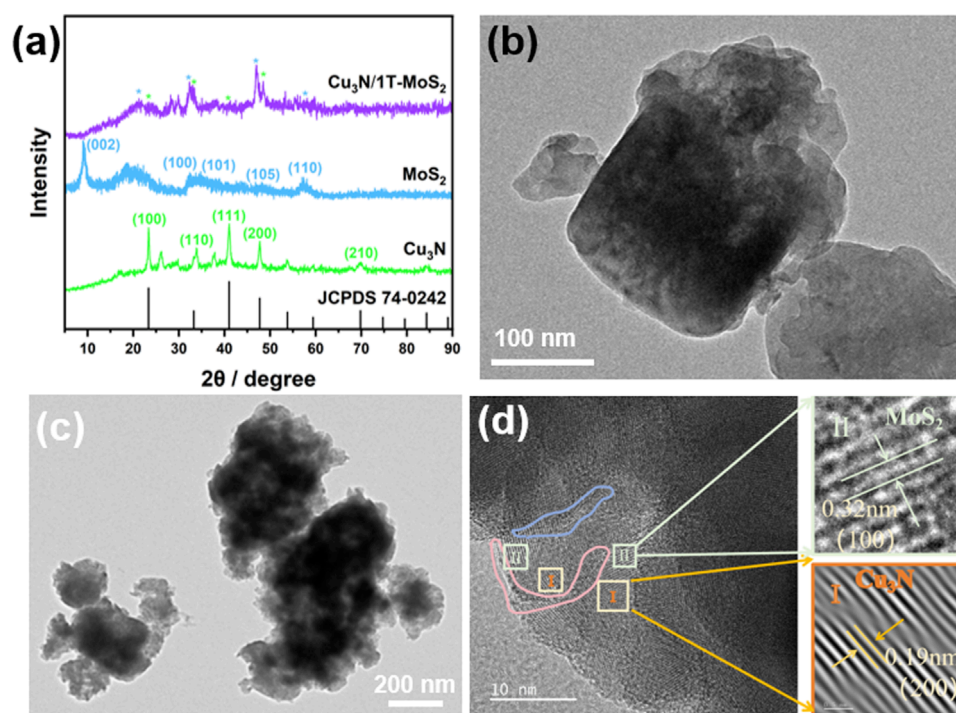


FIGURE 2 (a) XRD patterns of Cu_3N , MoS_2 and $\text{Cu}_3\text{N}/\text{MoS}_2(1:1)$. (b) TEM of Cu_3N . (c) TEM of $\text{Cu}_3\text{N}/\text{MoS}_2(1:1)$. (d) HRTEM of $\text{Cu}_3\text{N}/\text{MoS}_2(1:1)$ with characteristic lattice fringes.

Supplementary Figures S3a, b displays the selected-area electron-diffraction (SAED) pattern acquired from an individual Cu_3N nanocube, fully corroborating the XRD results (Figure 2a). The pattern shows discrete, azimuthally discontinuous spots arranged on concentric rings rather than continuous Debye-Scherrer rings (Jiang et al., 2014; Mallick et al., 2024; Mondal and Raj, 2018). This indicates that the probed area contains a limited number of well-oriented crystallites—consistent with monocrystalline cubes observed by TEM—rather than a random powder. The SAED analysis substantiates that the as-synthesized Cu_3N nanocubes are highly crystalline, phase-pure and possess long-range order—prerequisites for achieving intimate electronic contact and efficient charge transfer in the $\text{Cu}_3\text{N}/\text{MoS}_2$ heterostructures discussed in the subsequent sections. Supplementary Figures S3b presents the SAED pattern collected from a single $\text{Cu}_3\text{N}/\text{MoS}_2$ particle synthesized at the optimal $\text{Cu}_3\text{N}:\text{Mo}$ precursor ratio of 1:1. In contrast to the spot-like pattern of pristine Cu_3N (Supplementary Figures S3a), the composite exhibits a series of nearly continuous diffraction rings populated by discrete spots, reflecting the coexistence of a highly ordered Cu_3N core and a polycrystalline shell of few-layer MoS_2 nanosheets with random in-plane orientation. All diffraction maxima can be indexed exclusively to Cu_3N and metallic 1T- MoS_2 , confirming the phase purity inferred from XRD. The innermost rings ($2.6, 3.7, 4.5 \text{ nm}^{-1}$) are dominated by discrete spots rather than continuous arcs, indicative of a single-crystalline Cu_3N core whose zone axis is preserved across the illuminated area (Jayabal et al., 2018; Mallick et al., 2024; Mondal and Raj, 2018; Wang et al., 2020; Yu et al., 2018). In contrast, the

outer rings ($3.2, 5.2, 6.2 \text{ nm}^{-1}$) are quasi-continuous, signifying that the MoS_2 shell is composed of numerous nanoflakes with random azimuthal distribution—fully consistent with the radially oriented “rose-like” nanosheets observed in SEM/TEM. The SAED evidence validates the successful construction of a coherent $\text{Cu}_3\text{N}/1\text{T-MoS}_2$ core-shell heterostructure with intimate lattice contact and well-defined crystallographic orientation, underpinning the superior electrochemical performance.

The atomically intimate juxtaposition of the metallic 1T- MoS_2 flakes with the conductive Cu_3N core, together with the measured bidirectional strain, is expected to (i) enhance orbital overlap for interfacial electron transfer and (ii) modulate the d-band centre of MoS_2 , thereby optimising the adsorption free energy of reaction intermediates. Increasing the Mo precursor to the stoichiometric ratio yields a conformal, flower-like MoS_2 shell composed of radially aligned nanosheets. The original cubic outline remains discernible as a bright core in TEM, suggesting a core-shell rather than a yolk-shell arrangement. The tight interface and hierarchical porosity of this architecture rationalize its optimal electrochemical behaviour. A further increase in Mo results in excessive MoS_2 deposition. Thick, intergrown sheets envelop the cubes and protrude outward, forming an open network that partially detaches from the core. Such overgrowth is likely to impede charge transfer between the catalytic MoS_2 surface and the conductive Cu_3N core.

Across all hybrids, the observed lattice juxtaposition matches the compressive/tensile peak shifts detected by XRD, corroborating the presence of elastic lattice strain at the heterojunction. The TEM study verifies that controlled MoS_2 growth on Cu_3N proceeds via

an edge-selective nucleation mechanism, allowing precise tuning of shell thickness. The 1:1 composite offers the optimal compromise between interfacial area, electronic coupling and mass transport, providing a structural basis for the superior catalytic metrics.

XPS analysis confirms the formation of the Cu₃N/MoS₂ heterojunction through distinct interfacial electronic interactions (Figure 3 and Supplementary Figures S4). For pristine Cu₃N, Cu 2p peaks at 933.87 eV (Cu⁺ 2p_{3/2}) and 935.93 eV (Cu²⁺ 2p_{3/2}), along with the N 1s signal at 399.13 eV, are observed (Amiin et al., 2017; Mallick et al., 2024; Mondal and Raj, 2018; Zhu et al., 2020a), while in Cu₃N/MoS₂ these shift to 932.55 eV and 934.86 eV for Cu 2p_{3/2} and 399.39 eV for N 1s, indicating electron redistribution at the interface. For MoS₂, Mo 3d peaks at 229.02 eV/232.22 eV (1 T-Mo⁴⁺ 3d_{5/2} and 3d_{3/2}) and S 2p peaks at 161.98 eV/163.10 eV are characteristic of 1T-MoS₂, while in Cu₃N/MoS₂ the Mo 3d signals shift positively to 232.7 eV/235.7 eV and the S 2p peaks remain slightly perturbed. The opposite shifts of Cu and Mo binding energies demonstrate interfacial charge transfer between Cu₃N and MoS₂, consistent with p-n junction formation. These results, together with XRD and TEM evidence, confirm strong interfacial coupling and validate the construction of the Cu₃N/1 T-MoS₂ heterostructure. The observed charge transfer and chemical potential equilibration also align with the strain couple revealed by XRD/TEM, which is expected to modulate the d-band center of MoS₂, strengthen adsorption of intermediates, and facilitate interfacial electron delivery, thereby promoting HER kinetics.

HER activity was evaluated in 0.5 M H₂SO₄ (pH ≈ 0.34) using a standard three-electrode configuration (Ag/AgCl reference, graphite counter). All potentials were converted to the RHE scale according to $E_{(RHE)} = E_{(Ag/AgCl)} + 0.0592 \text{ pH} + 0.197$, and iR-drop was corrected by 90% unless otherwise noted. Polarization curves (LSV) and Tafel plots for pristine Cu₃N, pristine MoS₂ and Cu₃N/MoS₂ with feed ratios of 1:0.5, 1:1 and 1:2 are shown in Figure 4.

The overpotential required to deliver $j = 50 \text{ mA cm}^{-2}$ (η_{50}) and the Tafel slope extracted from the low-overpotential region are summarized in Figure 4. Consistent with the LSV traces (Figure 4a), the Cu₃N/MoS₂ (1:1) heterostructure exhibits the lowest η_{50} (387 mV), outperforming pristine MoS₂ (≈456 mV) and far exceeding Cu₃N, which shows negligible activity at this current density (Figures 4a,c). Increasing or decreasing the MoS₂ fraction from the 1:1 optimum degrades performance ($\eta_{50} = 417\text{--}455 \text{ mV}$) (Figure 4c), indicating that an appropriate Cu₃N-MoS₂ balance is crucial for maximizing accessible active sites and charge-transfer pathways. Long-term stability was assessed via chronopotentiometry at 387 mV of overpotential over 150 h (Figure 4d). The Cu₃N/MoS₂(1:1) electrode shows negligible performance decay, demonstrating excellent durability in acidic conditions.

In acidic media, canonical slopes of ≈120, ≈40 and ≈30 mV dec⁻¹ are typically associated with Volmer (H⁺ adsorption), Heyrovsky (electrochemical desorption) and Tafel rate-determining steps, respectively (Jacobson et al., 2022). The value of 57 mV dec⁻¹ for the 1:1 sample points to a Volmer–Heyrovsky mechanism, whereas pristine MoS₂ (105 mV dec⁻¹) is largely limited by the Volmer adsorption step (Figure 4b). The substantial reduction in Tafel slope for the 1:1 heterostructure signifies faster interfacial

charge transfer and more favorable H⁺ adsorption free energy (ΔG_{H^+}), in line with the electronic modulation inferred from XPS (electron flow from Cu₃N to MoS₂) and the coherent/strained interfaces resolved by XRD/TEM.

Electrochemical impedance spectroscopy (EIS) was carried out for Cu₃N, MoS₂, and Cu₃N/MoS₂ with varied ratios (Figure 5a). The Nyquist plots deviate from an ideal semicircle, likely due to the porous electrode, heterogeneous interfaces, and mixed kinetics-diffusion contributions (rather than a simple Randles circuit). Even so, the high-frequency intercepts and arc radii remain diagnostic of charge transfer. The Cu₃N/MoS₂ (1:1) sample shows the smallest arc radius, indicating the lowest Rct, which agrees with its lower overpotential, smaller Tafel slope, and superior durability. These results confirm that the 1:1 heterojunction affords the most effective interfacial coupling and fastest charge transport among the tested catalysts (Feng et al., 2022).

The electrochemically active surface area (ECSA) was estimated from the double-layer capacitance (C_{dl}) obtained by cyclic voltammetry in a non-Faradaic potential window at various scan rates. The slope of the capacitive current density (Δj) versus scan rate plot yields C_{dl} values (Figure 5b). The C_{dl} of Cu₃N/MoS₂(1:1) is ~25× larger than that of pristine Cu₃N and markedly higher than those of the other composites, signifying a dramatic increase in accessible active sites. This enhancement originates from the hierarchical core-shell morphology and ultrathin MoS₂ nanosheets observed in SEM/TEM, which expose abundant edge sites while preserving open ion-transport channels. To further evaluate the intrinsic catalytic activity, LSV curves normalized to the electrochemical surface area (ECSA) were recorded (Supplementary Figure S6). The ECSA-normalized activity sequence follows Cu₃N/MoS₂(1:1) < Cu₃N/MoS₂(1:0.5) < Cu₃N/MoS₂ (1:2) (under 0.1 mA cm⁻²), indicating that the 1:2 composite delivers the highest intrinsic activity per active site. However, the conventional LSV (Figure 4a) shows the order Cu₃N/MoS₂(1:2) < Cu₃N/MoS₂(1:0.5) < Cu₃N/MoS₂(1:1) (under 50 mA cm⁻²), demonstrating that the 1:1 composite exhibits the best overall apparent performance. This difference arises because ECSA normalization highlights intrinsic activity per site, whereas the conventional curves reflect both site activity and the density of accessible active sites. Thus, although Cu₃N/MoS₂(1:2) features highly active sites, its relatively limited surface area reduces the overall current density. In contrast, Cu₃N/MoS₂(1:1) achieves an optimal balance between intrinsic activity and accessible sites, leading to the best overall HER performance. These findings confirm that the synergistic p–n interfacial coupling not only enhances site activity but also optimizes charge transport and site accessibility, together underpinning the superior HER performance of Cu₃N/1T-MoS₂.

The EIS and C_{dl} results together demonstrate that the superior HER activity of Cu₃N/MoS₂(1:1) stems from a dual benefit: (i) enhanced interfacial charge transfer, facilitated by strong electronic coupling and lattice-matched interfaces between Cu₃N and MoS₂; and (ii) maximised ECSA, arising from the optimal MoS₂ coverage that prevents both under-exposure of catalytic edges (as in low-Mo samples) and blockage of conductive pathways (as in high-Mo samples). These synergistic effects explain why the 1:1 heterostructure achieves the best performance metrics across all electrochemical analyses.

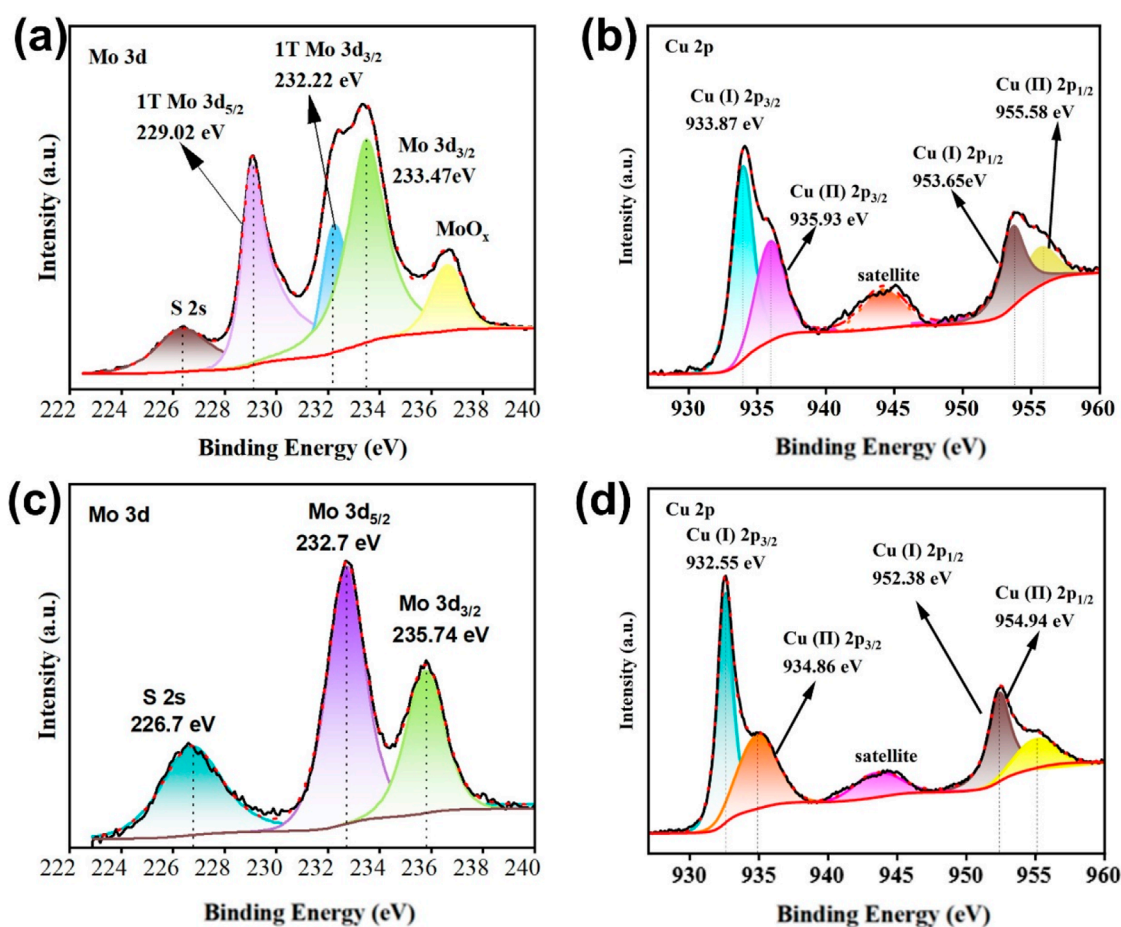


FIGURE 3

XPS of Cu_3N , MoS_2 and $\text{Cu}_3\text{N}/\text{MoS}_2$. (a) Mo 3d spectrum of MoS_2 . (b) Cu 2p spectrum of Cu_3N . (c) Mo 3d spectrum of $\text{Cu}_3\text{N}/\text{MoS}_2$. (d) Cu 2p spectrum of $\text{Cu}_3\text{N}/\text{MoS}_2$.

The band-edge positions of p-type Cu_3N and n-type MoS_2 were determined by combining diffuse reflectance spectroscopy (DRS), Mott–Schottky (M–S) analysis, and valence band (VB) XPS measurements, enabling precise construction of their energy level diagrams relative to RHE.

From the Tauc plots (Figures 6a,b), the optical band gaps (E_g) were extracted as 1.12 eV for MoS_2 and 1.34 eV for Cu_3N (Feng et al., 2015; Makuła et al., 2018). Mott–Schottky plots (Figures 6c,d) recorded at different frequencies exhibit opposite slopes, confirming the p-type semiconductor of Cu_3N and the n-type semiconductor of MoS_2 (Gelderman et al., 2007; Sivula, 2021; Xu et al., 2022). The flat-band potentials (E_{fb}) were determined to be +1.59 V (vs. RHE) for Cu_3N and +0.116 V (vs. RHE) for MoS_2 . For p-type Cu_3N , the VB maximum (VBM) lies slightly below E_{fb} (≈ 0.2 eV), giving $E_{VB} \approx +1.79$ V vs. RHE. For n-type MoS_2 , E_{fb} approximates the conduction band minimum (CBM), thus $E_{CB} \approx -0.08$ V (vs. RHE). According to $E_{CB} = E_{VB} - E_g$, the E_{CB} of Cu_3N and E_{VB} of MoS_2 are 0.45 V and 1.04 V (vs. RHE), respectively.

On the basis of the foregoing analysis, a plausible catalytic mechanism was elucidated. The $\text{Cu}_3\text{N}/\text{MoS}_2$ heterojunction was constructed via intimate contact between Cu_3N nanostructures and layered MoS_2 , forming a p–n charge transfer pathway (Scheme 1).

(Dai et al., 2024; Li and Zhou, 2021; Li et al., 2025; Qin et al., 2023; Zhu et al., 2020a; Zhu et al., 2020b) Upon contact, the difference in Fermi levels drives electrons from MoS_2 to Cu_3N , resulting in electron accumulation on the Cu_3N side and hole accumulation on the MoS_2 side. This interfacial charge redistribution generates a built-in electric field across the junction, inducing upward bending of MoS_2 bands and downward bending of Cu_3N bands until thermodynamic equilibrium is reached. Such an internal field has been widely recognized to facilitate charge separation and directional migration in heterojunction electrocatalysts.

Under cathodic polarization, electrons are preferentially injected into the MoS_2 conduction band, where they participate in the Volmer step ($\text{H}^+ + \text{e}^- \rightarrow \text{H}^*$) on exposed S-edge/Mo-center sites, followed by either the Heyrovsky ($\text{H}^* + \text{H}^+ + \text{e}^- \rightarrow \text{H}_2$) or Tafel ($2\text{H}^* \rightarrow \text{H}_2$) step. Simultaneously, bias-driven holes are directed towards Cu_3N and consumed via the external circuit, effectively suppressing charge recombination. The synergistic action of the internal field and external bias thus ensures spatial separation of electrons (localized in MoS_2 -CB) and holes (localized in Cu_3N -VB).

Electrochemical impedance spectroscopy (EIS) measurements demonstrate that the $\text{Cu}_3\text{N}/\text{MoS}_2$ electrode exhibits a markedly

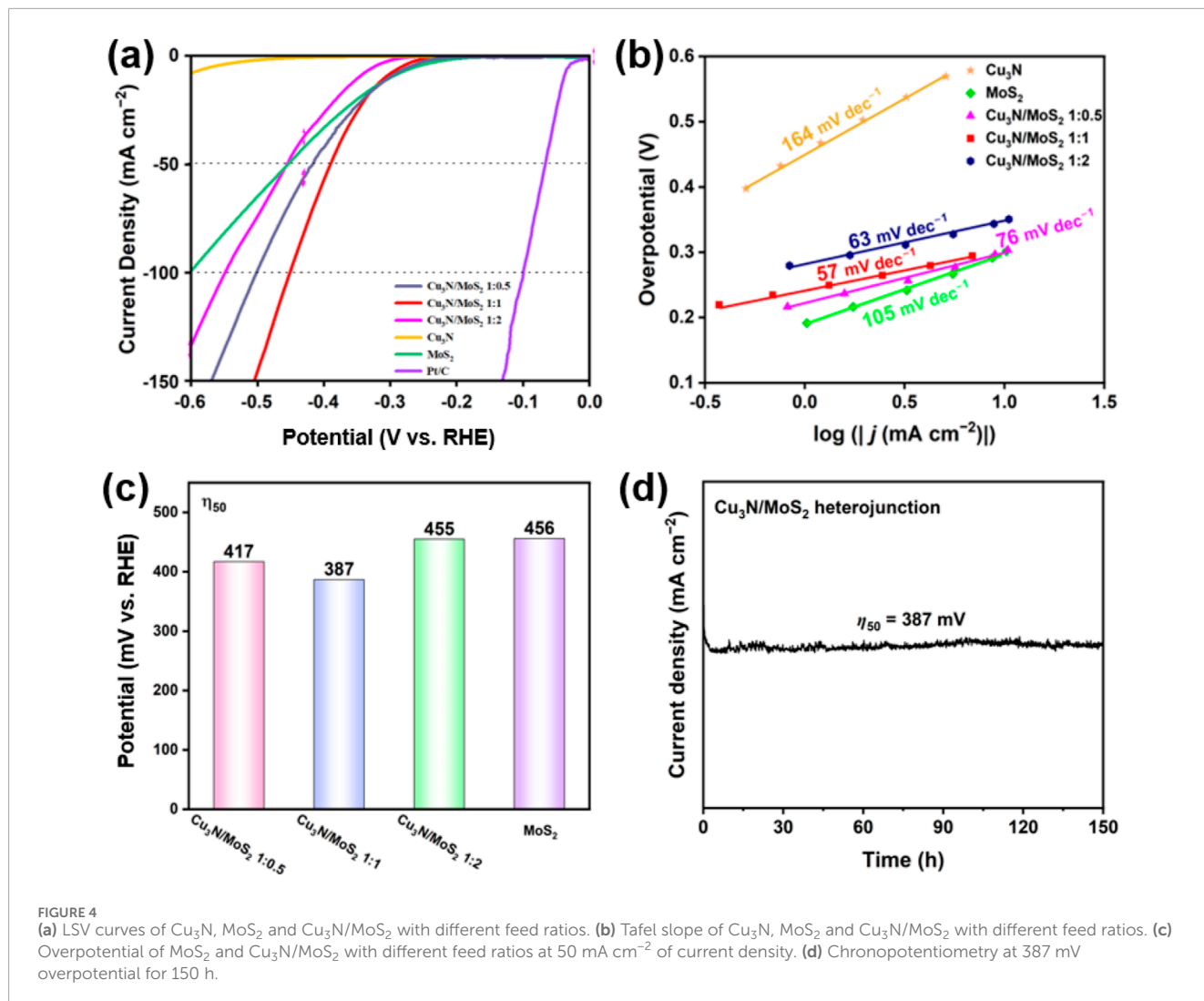


FIGURE 4 (a) LSV curves of Cu_3N , MoS_2 and $\text{Cu}_3\text{N}/\text{MoS}_2$ with different feed ratios. (b) Tafel slope of Cu_3N , MoS_2 and $\text{Cu}_3\text{N}/\text{MoS}_2$ with different feed ratios. (c) Overpotential of MoS_2 and $\text{Cu}_3\text{N}/\text{MoS}_2$ with different feed ratios at 50 mA cm^{-2} of current density. (d) Chronopotentiometry at 387 mV overpotential for 150 h.

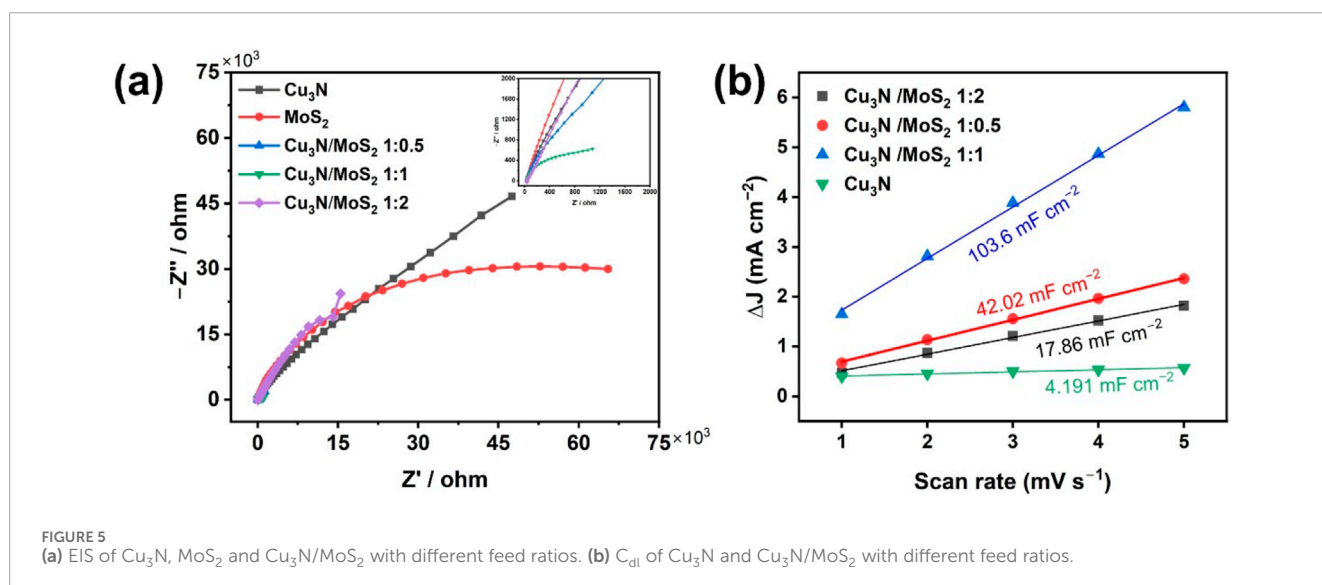


FIGURE 5 (a) EIS of Cu_3N , MoS_2 and $\text{Cu}_3\text{N}/\text{MoS}_2$ with different feed ratios. (b) C_{dl} of Cu_3N and $\text{Cu}_3\text{N}/\text{MoS}_2$ with different feed ratios.

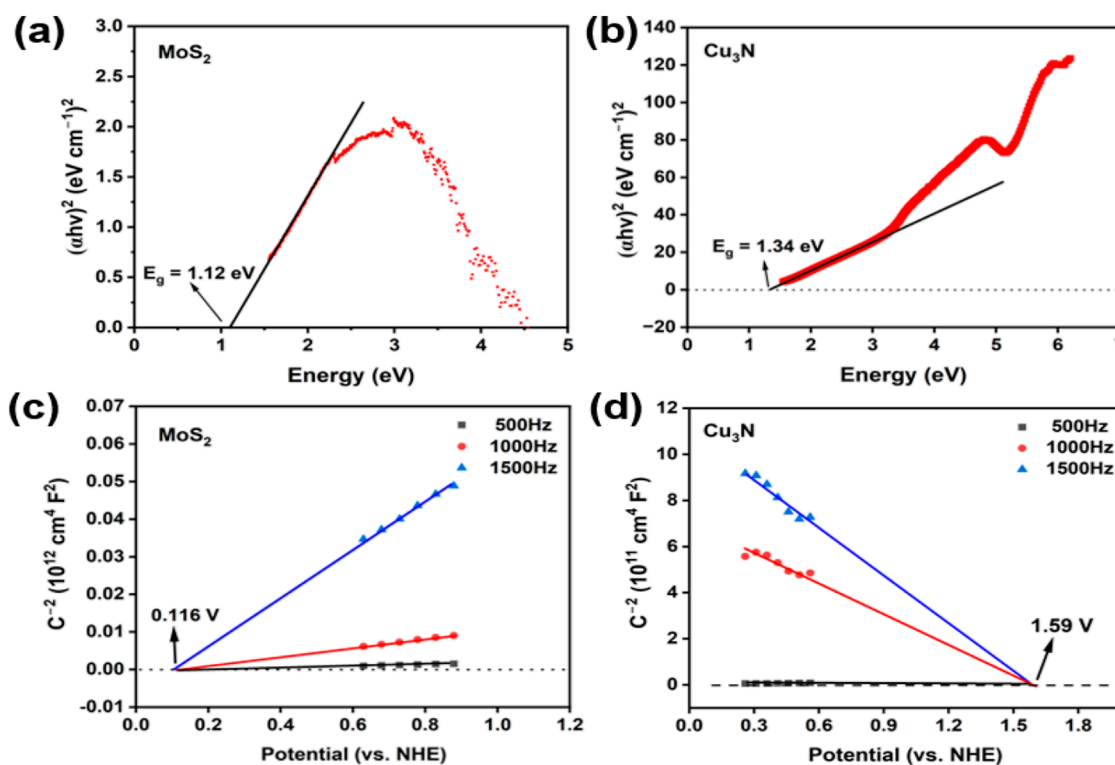
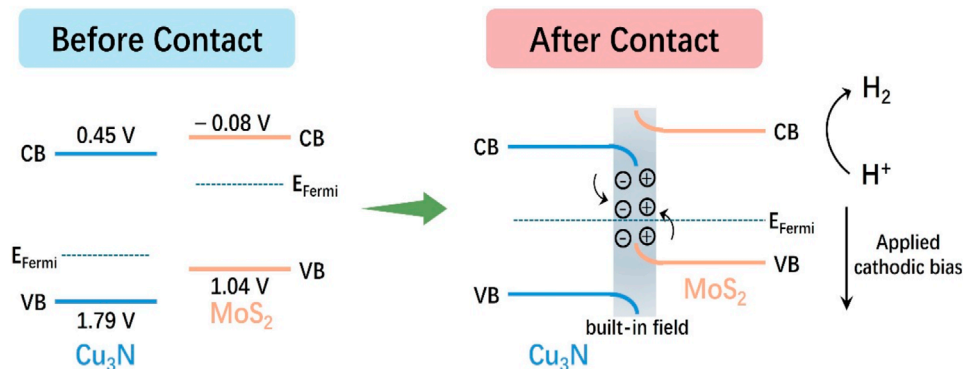


FIGURE 6 Tauc plots of (a) MoS₂ and (b) Cu₃N. Mott-Schottky plots of (c) MoS₂ and (d) Cu₃N at different frequency.



SCHEME 1 The mechanism of Cu₃N/MoS₂ of electrocatalytic hydrogen evolution.

reduced charge-transfer resistance (R_{ct}) compared to pristine components, while double-layer capacitance (C_{dl}) measurements reveal an increased electrochemically active surface area (ECSA). These results confirm accelerated charge transport and higher active site density, consistent with the lower Tafel slope and higher turnover frequency observed. The hierarchical architecture further facilitates electrolyte penetration and rapid release of evolved H₂, maintaining high catalytic activity and stability under large current densities.

The Cu₃N/1 T-MoS₂ heterojunction delivers a balanced acidic-HER performance, combining a low overpotential at practical current density ($\eta_{50} = 387$ mV; Tafel = 57 mV dec⁻¹), 150 h durability, and robust operation in 0.5 M H₂SO₄ (comparison [Supplementary Table S1](#)). This co-optimization stems from a p-n built-in field that drives directional charge separation, noble-metal-free electronic wiring from Cu₃N, and interfacial stabilization of the 1 T phase. The straightforward synthesis and interfacial durability further support scale-up and device integration.

4 Conclusion

In conclusion, we have developed an interface-engineered Cu₃N/I T-MoS₂ heterojunction that couples conductive p-type Cu₃N nanocubes with ultrathin MoS₂ nanosheets. The composite achieves 387 mV at 50 mA cm⁻² with a 57 mV dec⁻¹ Tafel slope in 0.5 M H₂SO₄ and maintains performance for 150 h. Structure–property correlation shows: (i) coherent interfaces and interfacial strain verified by XRD/TEM; (ii) XPS-evidenced charge redistribution; (iii) lowest R_{ct} and highest C_{dl} (up to 103.6 mF cm⁻²) among all samples, indicating rapid charge transport and abundant active sites. The activity enhancement is thus attributed to a p–n heterojunction with a built-in electric field, which funnels electrons toward MoS₂ edge sites while suppressing recombination. This study positions Cu₃N as a versatile platform for stabilizing conductive MoS₂ and offers generalizable design guidelines for interfacial-coupled HER electrocatalysts operating in acidic media.

Data availability statement

The original contributions presented in the study are included in the article/Supplementary Material, further inquiries can be directed to the corresponding authors.

Author contributions

TH: Validation, Methodology, Investigation, Writing – original draft. WX: Conceptualization, Investigation, Supervision, Funding acquisition, Writing – review and editing, Project administration, Data curation, Methodology, Validation. FJ: Writing – review and editing. VP: Writing – review and editing. QZ: Writing – review and editing, Methodology, Formal analysis. SK: Writing – review and editing, Methodology, Formal analysis. AY: Writing – review and editing.

Funding

The author(s) declare that financial support was received for the research and/or publication of this article. This work was

References

- Amiin, I. S., Pu, Z., Liu, X., Owusu, K. A., Monestel, H. G. R., Boakye, F. O., et al. (2017). Multifunctional Mo–N/C@MoS₂ electrocatalysts for HER, OER, ORR, and Zn–Air batteries. *Adv. Funct. Mater.* 27 (44), 1702300. doi:10.1002/adfm.201702300
- Ayodele, B. V., Mustapa, S. I., Abdullah, T. A. R. B. T., and Salleh, S. F. S. F. (2019). A mini-review on hydrogen-rich syngas production by thermo-catalytic and bioconversion of biomass and its environmental implications. *Front. Energy Res.* 7, 118. doi:10.3389/fenrg.2019.00118
- Boretti, A., Nayfeh, J., and Al-Maaitah, A. (2021). Hydrogen production by solar thermochemical water-splitting cycle via a beam down concentrator. *Front. Energy Res.* 9, 666191. doi:10.3389/fenrg.2021.666191
- Chia, X., Eng, A. Y. S., Ambrosi, A., Tan, S. M., and Pumera, M. (2015). Electrochemistry of nanostructured layered transition-metal dichalcogenides. *Chem. Rev.* 115 (21), 11941–11966. doi:10.1021/acs.chemrev.5b00287
- Chiu, N. C., Lessard, J. M., Musa, E. N., Lancaster, L. S., Wheeler, C., Krueger, T. D., et al. (2024). Elucidation of the role of metals in the adsorption and photodegradation of

financially supported by the Natural Science Foundation of Hunan Province (No.2024JJ7407), Outstanding Youth Foundation of Hunan Provincial Education Department (No.23B0503), Scientific research start-up funding of Jishou university, which were greatly appreciated.

Conflict of interest

The authors declare that the research was conducted in the absence of any commercial or financial relationships that could be construed as a potential conflict of interest.

Generative AI statement

The author(s) declare that no Generative AI was used in the creation of this manuscript.

Any alternative text (alt text) provided alongside figures in this article has been generated by Frontiers with the support of artificial intelligence and reasonable efforts have been made to ensure accuracy, including review by the authors wherever possible. If you identify any issues, please contact us.

Publisher's note

All claims expressed in this article are solely those of the authors and do not necessarily represent those of their affiliated organizations, or those of the publisher, the editors and the reviewers. Any product that may be evaluated in this article, or claim that may be made by its manufacturer, is not guaranteed or endorsed by the publisher.

Supplementary material

The Supplementary Material for this article can be found online at: <https://www.frontiersin.org/articles/10.3389/fenrg.2025.1683318/full#supplementary-material>

herbicides by metal-organic frameworks. *Nat. Commun.* 15, 1459. doi:10.1038/s41467-024-45546-y

Dai, M., Zhang, T., Huang, J., Lang, X., Li, Q., Zou, J., et al. (2024). Construction of a pp heterojunction Co₃O₄/MoS₂ electrocatalyst for boosting hydrogen evolution reaction. *Electrochimica Acta* 494, 144451. doi:10.1016/j.electacta.2024.144451

Du, L., Xiong, H., Lu, H., Yang, L. M., Liao, R. Z., Xia, B. Y., et al. (2022). Electroshock synthesis of a bifunctional nonprecious multi-element alloy for alkaline hydrogen oxidation and evolution. *Pap. Present. A. T. Explor.* 2, 20220024. doi:10.1002/exp.20220024

Feng, Y., Lin, S., Huang, S., Shrestha, S., and Conibeer, G. (2015). Can tauc plot extrapolation be used for direct-band-gap semiconductor nanocrystals? *J. Appl. Phys.* 117 (12), 125701. doi:10.1063/1.4916090

Feng, Y., Guan, Y., Zhou, E., Zhang, X., and Wang, Y. (2022). Nanoscale double-heterojunctional electrocatalyst for hydrogen evolution. *Adv. Sci.* 9 (18), 2201339. doi:10.1002/advs.202201339

- Gan, L., Lai, J., Liu, Z., Luo, J., Zhang, S., and Zhang, Q. (2022). Interfacial engineering of heterojunction copper-cobalt-nickel nitride as binder-free electrode for efficient water splitting. *J. Alloys Compd.* 905, 164200. doi:10.1016/j.jallcom.2022.164200
- Gelderman, K., Lee, L., and Donne, S. W. (2007). Flat-band potential of a semiconductor: using the mott-schottky equation. *J. Chem. Educ.* 84 (4), 685. doi:10.1021/ed084p685
- Gong, F., Liu, Y., Zhao, Y., Liu, W., Zeng, G., Wang, G., et al. (2023). Universal sub-nanoreactor strategy for synthesis of yolk-shell MoS₂ supported single atom electrocatalysts toward robust hydrogen evolution reaction. *Angew. Chem. Int. Ed.* 62 (40), e202308091. doi:10.1002/ange.202308091
- Jacobson, M. Z., Krauland, A.-K. v., Coughlin, S. J., Dukas, E., Nelson, A. J. H., Palmer, F. C., et al. (2022). Low-cost solutions to global warming, air pollution, and energy insecurity for 145 countries. *Energy and Environ. Sci.* 15 (8), 3343–3359. doi:10.1039/d2ee00722c
- Jayabal, S., Wu, J., Chen, J., Geng, D., and Meng, X. (2018). Metallic 1T-MoS₂ nanosheets and their composite materials: preparation, properties and emerging applications. *Mater. Energy* 10, 264–279. doi:10.1016/j.mtener.2018.10.009
- Jiang, X., Wu, K., Shao, L., Shui, M., Lin, X., Lao, M., et al. (2014). Lithium storage mechanism in superior high capacity copper nitrate hydrate anode material. *J. Power Sources* 260, 218–224. doi:10.1016/j.jpowsour.2014.03.021
- Jin, H., Zhang, Y., Cao, Z., Liu, J., and Ye, S. (2025). Atomically dispersed Sn on core-shell MoS₂ nanoreactors as mott-schottky phase junctions for efficient electrocatalytic hydrogen evolution. *Adv. Mater.* 37 (33), 2502977. doi:10.1002/adma.202502977
- Kwon, H. R., Yang, J. W., and Jang, H. W. (2025). Metal nitride catalysts for photoelectrochemical and electrochemical catalysis. *Pap. Present. Explor.* 5, 20240013. doi:10.1002/exp.20240013
- Li, J., and Zhou, X. (2021). First principles calculations of electrical and optical properties of Cu₃N/MoS₂ heterostructure with tunable bandgaps. *Appl. Phys. A* 127, 693. doi:10.1007/s00339-021-04858-2
- Li, X., Hao, X., Abudula, A., and Guan, G. (2016). Nanostructured catalysts for electrochemical water splitting: current state and prospects. *J. Mater. Chem. A* 4 (31), 11973–12000. doi:10.1039/c6ta02334g
- Li, L., Wang, P., Shao, Q., and Huang, X. (2020). Metallic nanostructures with low dimensionality for electrochemical water splitting. *Chem. Soc. Rev.* 49 (10), 3072–3106. doi:10.1039/d0cs00013b
- Li, X., Guan, H., and Mu, Z. (2025). DFT study of a promising water splitting photocatalyst: Cu₃N/MoS₂ heterojunction. *J. Electron. Mater.* 54, 2921–2929. doi:10.1007/s11664-025-11769-y
- Liu, Y., Jiang, S., Li, S., Zhou, L., Li, Z., Li, J., et al. (2019). Interface engineering of (Ni, Fe)S₂@MoS₂ heterostructures for synergistic electrochemical water splitting. *Appl. Catal. B Environ.* 247, 107–114. doi:10.1016/j.apcatb.2019.01.094
- Liu, S., Zhou, L., Zhang, W., Jin, J., Mu, X., Zhang, S., et al. (2020). Stabilizing sulfur vacancy defects by performing “click” chemistry of ultrafine palladium to trigger a high-efficiency hydrogen evolution of MoS₂. *Nanoscale* 12 (18), 9943–9949. doi:10.1039/d0nr01693d
- Makula, P., Pacia, M., and Macyk, W. (2018). How to correctly determine the band gap energy of modified semiconductor photocatalysts based on UV-Vis spectra. *J. Phys. Chem. Lett.* 9 (23), 6814–6817. doi:10.1021/acs.jpclett.8b02892
- Mallick, B., Rajak, A., Giri, S., Behera, L., Parija, B., Mallick, P., et al. (2024). A new technique for synthesis of the Cu₃N and its structural indexing. *Indian J. Phys.* 98, 4039–4051. doi:10.1007/s12648-024-03178-4
- McHugh, P. J., Stergiou, A. D., and Symes, M. D. (2020). Decoupled electrochemical water splitting: from fundamentals to applications. *Adv. Energy Mater.* 10 (44), 2002453. doi:10.1002/aenm.202002453
- Meshesha, M. M., Gautam, J., Chanda, D., Jang, S. G., and Yang, B. L. (2023). Enhancing the electrochemical activity of zinc cobalt sulfide via heterojunction with MoS₂ metal phase for overall water splitting. *J. Colloid Interface Sci.* 652, 272–284. doi:10.1016/j.jcis.2023.08.005
- Miao, L., Jia, W., Cao, X., and Jiao, L. (2024). Computational chemistry for water-splitting electrocatalysis. *Chem. Soc. Rev.* 53 (6), 2771–2807. doi:10.1039/D2CS01068B
- Mondal, S., and Raj, C. R. (2018). Copper nitride nanostructure for the electrocatalytic reduction of oxygen: kinetics and reaction pathway. *J. Phys. Chem. C* 122 (32), 18468–18475. doi:10.1021/acs.jpcc.8b03840
- Qin, M., Chen, L., Zhang, H., Humayun, M., Fu, Y., Xu, X., et al. (2023). Achieving highly efficient pH-universal hydrogen evolution by Mott-Schottky heterojunction of Co₂P/Co₄N. *Chem. Eng. J.* 454, 140230. doi:10.1016/j.cej.2022.140230
- Rao, T., Wang, H., Zeng, Y.-J., Guo, Z., Zhang, H., and Liao, W. (2021). Phase transitions and water splitting applications of 2D transition metal dichalcogenides and metal phosphorous trichalcogenides. *Adv. Sci.* 8 (10), 2002284. doi:10.1002/advs.202002284
- Sivula, K. (2021). Mott-Schottky analysis of photoelectrodes: sanity checks are needed. *ACS Energy Lett.* 6 (7), 2549–2551. doi:10.1021/acscenergylett.1c01245
- Sun, H., Xu, X., Kim, H., Jung, W., Zhou, W., and Shao, Z. (2023). Electrochemical water splitting: bridging the gaps between fundamental research and industrial applications. *Energy and Environ. Mater.* 6 (5), e12441. doi:10.1002/eem2.12441
- Sun, H., Xu, X., Song, Y., Zhou, W., and Shao, Z. (2021). Designing high-valence metal sites for electrochemical water splitting. *Adv. Funct. Mater.* 31 (16), 2009779. doi:10.1002/adfm.202009779
- Sun, Y., Xu, S., Ortíz-Ledón, C. A., Zhu, J., Chen, S., and Duan, J. (2021). Biomimetic assembly to superplastic metal-organic framework aerogels for hydrogen evolution from seawater electrolysis. *Pap. Present. A. T. Explor.* 1, 20210021. doi:10.1002/exp.20210021
- Vasiladiou, I. A., Berná, A., Manchon, C., Meleró, J. A., Martínez, F., Esteve-Núñez, A., et al. (2018). Biological and bioelectrochemical systems for hydrogen production and carbon fixation using purple phototrophic bacteria. *Front. Energy Res.* 6, 107. doi:10.3389/fenrg.2018.00107
- Wang, J., Fang, W., Hu, Y., Zhang, Y., Dang, J., Wu, Y., et al. (2020). Different phases of few-layer MoS₂ and their silver/gold nanocomposites for efficient hydrogen evolution reaction. *Catal. Sci. and Technol.* 10 (1), 154–163. doi:10.1039/c9cy02158b
- Wang, J., Liu, Z., Dai, Z., Song, X., and Liu, X. (2023). Multifunctional catalytic activity of Cu₃N (001) surface: a first-principles study. *ChemPhysMater* 2 (3), 231–238. doi:10.1016/j.chphma.2022.10.001
- Wang, L., Zhang, C., Cao, Z., Zeng, G., Liu, J., and Ye, S. (2024). Dual modulation of bulk electronic structure and surficial active sites in sea urchin-like MoO₃ nanoreactors promoting electrocatalytic hydrogen evolution. *Adv. Funct. Mater.* 34 (42), 2406670. doi:10.1002/adfm.202406670
- Xu, D., Zhang, S.-N., Chen, J.-S., and Li, X.-H. (2022). Design of the synergistic rectifying interfaces in Mott-Schottky catalysts. *Chem. Rev.* 123 (1), 1–30. doi:10.1021/acs.chemrev.2c00426
- Xue, H., Meng, A., Chen, C., Xue, H., Li, Z., and Wang, C. (2022). Phosphorus-doped MoS₂ with sulfur vacancy defects for enhanced electrochemical water splitting. *Sci. China Mater.* 65, 712–720. doi:10.1007/s40843-021-1774-9
- Yu, Y., Nam, G. H., He, Q., Wu, X.-J., Zhang, K., Yang, Z., et al. (2018). High phase-purity 1T'-MoS₂- and 1T'-MoSe₂-layered crystals. *Nat. Chem.* 10, 638–643. doi:10.1038/s41557-018-0035-6
- Zhang, K., Ai, Z., Huang, M., Shi, D., Shao, Y., Hao, X., et al. (2021). Type II cuprous oxide/graphitic carbon nitride p-n heterojunctions for enhanced photocatalytic nitrogen fixation. *J. Catal.* 395, 273–281. doi:10.1016/j.jcat.2021.01.013
- Zhu, L., Cao, X., Gong, C., Jiang, A., Cheng, Y., and Xiao, J. (2020a). Preparation of Cu₃N/MoS₂ heterojunction through magnetron sputtering and investigation of its structure and optical performance. *Materials* 13 (8), 1873. doi:10.3390/ma13081873
- Zhu, L., Gong, C., Xiao, J., and Wang, Z. (2020b). Photocatalytic properties of copper nitride/molybdenum disulfide composite films prepared by magnetron sputtering. *Coatings* 10 (1), 79. doi:10.3390/coatings10010079